Aerospace Science and Technology ••• (••••) ••••••

Contents lists available at ScienceDirect

Aerospace Science and Technology

www.elsevier.com/locate/aescte

Intelligent sensitivity analysis framework based on machine learning for spacecraft thermal design

Yan Xiong [a,b], Liang Guo [a,*], Yuting Yang [a,b], Hongliang Wang [a,b]

[a] *Changchun Institute of Optics, Fine Mechanics and Physics, Chinese Academy of Sciences, Changchun, 130033, China*
[b] *University of Chinese Academy of Sciences, 100049, Beijing, China*

ARTICLE INFO

Article history:
Received 30 June 2020
Received in revised form 22 June 2021
Accepted 26 June 2021
Available online xxxx
Communicated by Z. Weiwei

Keywords:
Global sensitivity analysis
Spacecraft thermal design
Machine learning
Multi-fidelity

ABSTRACT

The variance-based method of global sensitivity analysis (GSA) has been widely applied in spacecraft thermal design, which is typically calculated using Monte Carlo estimations. However, such estimations require a large number of samples to ensure sufficient accuracy, which makes GSA expensive to perform when modeling is difficult. Moreover, multimodal or highly skewed output distributions may result in the use of variance as an uncertain agent that generates contradictory results. Therefore, an intelligent density-based GSA framework based on machine learning and multi-fidelity metamodels called IDGSA-3M is proposed. An intelligent batch processing system based on a real-time data interaction between MATLAB and NX/TMG was designed that uses many cheap low-fidelity sample points to reduce the cost of model evaluation while using a small number of expensive high-fidelity sample points to maintain high accuracy, thus achieving trade-offs between high accuracy and low computational cost. A radial basis function (RBF) neural network based on an improved mind evolutionary algorithm was applied to approximate the multi-fidelity metamodel of a spacecraft thermophysical model calculated using a batch processing system, which had a computational speed that was 1000+ times faster than that of the traditional thermophysical model and a high computational accuracy of 99%+. The output distributions of the RBF were then characterized by its cumulative distribution functions to obtain density-based sensitivity indices. Both the theoretical and experimental results of GSA for the thermal design parameters of the extreme ultraviolet radiation detector on the space-based Lyman-Alpha Solar Telescope, developed in China, demonstrated that the convergence rate of IDGSA-3M can be improved up to 10-fold for a fixed convergence level in comparison with two other GSA methods, thereby verifying its superiority.

1. Introduction

Global sensitivity analysis (GSA) is a set of mathematical methods based on statistics designed to gain insight into the relative contributions of different sources of uncertainty in model outputs [1–6]. GSA is increasingly and widely used in various engineering applications, particularly spacecraft thermal design optimization, which has expensive thermophysical models and many hyperparameters. GSA is almost indispensable for improving the efficiency of optimization and reducing the mean squared error (MSE) [7–9].

Spacecraft thermal design optimization requires a large amount of space thermal analysis to achieve appropriate thermal control effects. They are time-consuming finite element analysis (FEA) processes based on solving partial differential equations [10–13]. Many metamodeling approaches exist, which are known as approximation models or surrogate models that supersede the original model, which are used to improve computational efficiency, including the Kriging model [14–17], RBF [18], artificial neural network (ANN) [19,20], support vector regression (SVR) [21], and response surface methodology [22], which have been widely used in the field of optimization for spacecraft thermal design. However, these approaches require many high-fidelity (HF) samples to ensure that the metamodel has sufficient precision, and they take a great deal of time.

Multi-fidelity (MF) metamodeling approaches have attracted significant attention recently for data regression because they can trade-off between high accuracy and low computational expense by integrating the information from HF and low-fidelity (LF) models [23]. For example, the co-Kriging metamodel is a promising tool for building such an MF metamodel when the simulation models can be run at different levels of accuracy [24,25]. Gratiet et al. [24] obtained the hyperparameters of the co-Kriging metamodel by

---

[*] Corresponding author.
E-mail address: guoliang@ciomp.ac.cn (L. Guo).

https://doi.org/10.1016/j.ast.2021.106927
1270-9638/© 2021 Published by Elsevier Masson SAS.

Please cite this article as: Y. Xiong, L. Guo, Y. Yang et al., Intelligent sensitivity analysis framework based on machine learning for spacecraft thermal design, Aerospace Science and Technology, https://doi.org/10.1016/j.ast.2021.106927

minimizing the likelihood function according to the Markov property. However, sample points with different fidelities should be nested to allow a simple estimation of the model parameters for the co-Kriging metamodel [24]. Han and Görtz [26] proposed the hierarchical kriging approach, in which the LF model was taken as a model trend of the HF model. Scaling-function-based MF metamodel approaches, including multiplicative scaling approaches [27,28], additive scaling approaches [13,14,26], and hybrid scaling approaches [29,30], are also commonly used in engineering design optimization. In this paper, a neural network surrogate modeling approach based on MF metamodeling is proposed, which aims to improve the speed of the original model evaluation while ensuring the high prediction accuracy of the metamodel, which will benefit GSA.

One of the most widely used GSA methods is the variance-based method, which quantifies the relative effect of input parameters on model outputs by calculating the sensitivity index [31–35]. However, variance-based GSA is obtained from Monte Carlo integrals, which require enormous model sampling and numerous evaluations to obtain sufficient accuracy [36–38]. Moreover, multimodal or highly skewed output distributions may result in the use of variance as an uncertain agent that may generate contradictory results [39,40]. These limitations have stimulated a number of studies on “moment-independent” sensitivity indices, that is, indices that do not use a specific moment of the output distribution to characterize uncertainty and therefore are applicable independently of the shape of the distribution. These methods are sometimes referred to as “density-based” methods because they investigate the probability density function (PDF) of the model output rather than its variance only. In this case, sensitivity is related to the variations in the output PDF that are induced when removing uncertainty about one input. Entropy-based sensitivity measures [41–43] and the d-sensitivity measure [44,45] follow this line of reasoning.

Additionally, to mitigate the above-mentioned problems, several scholars have proposed various novel and efficient GSA methods, such as the classical variance-based GSA. Qian proposed a novel GSA method based on a MF Monte Carlo estimation (referred to as MFGSA) [46] and Pianos designed a GSA method (referred to as PAWN) that estimates the sensitivity analysis index by analyzing the cumulative distribution function (CDF) [47]. These methods are difficult to implement and apply in spacecraft thermal design optimization, which still mainly uses manual corrections of the thermal design parameters. Stout [48] and Thunnissen [49] proposed Bayesian-based thermal modeling to improve the effect of spacecraft thermal design optimization, but the computational efficiency was poor.

To solve these problems and obtain efficient and accurate GSA indices, an intelligent density-based GSA framework based on machine learning and MF called IDGSA-3M (IDGSA: intelligent density-based GSA framework; 3M: machine learning and MF metamodels) is proposed. This is the first time that density-based GSA has been applied to spacecraft thermal design optimization. Additionally, IDGSA-3M is different from traditional GSA approaches to spacecraft thermal design optimization computed using the time-consuming Monte Carlo estimation. It involves an intelligent batch processing system based on a real-time data interaction between MATLAB and NX/TMG, and uses LF models to reduce the computational cost of GSA while using HF models to maintain accuracy. The function of this system is to automatically evaluate the model based on sample input combinations within their variability space without supervision. The system is at least five times faster than traditional manual Monte Carlo estimates. The RBF neural network based on an improved mind evolutionary algorithm (IMEA) proposed by He et al. and Yanqing [50,51] is one of the most important effective hybrid strategies based on ANNs used to approximate nonlinear systems, and can speed up model convergence and avoid the disadvantage of falling into local optima in traditional RBF neural networks. It is applied to approximate the thermophysical model of spacecraft calculated using the batch processing system, and then the output distributions of the RBF are characterized by CDFs instead of probability distribution functions (PDFs) to obtain density-based GSA. Moreover, the approximate values of the empirical CDFs obtained from the data samples do not require cost calculations or tuning parameters. The results provided below demonstrate that the proposed method can effectively identify the impact of uncertain inputs on outputs and reduce the MSE of the estimator while using fewer model evaluations.

The remainder of this paper is organized as follows: In Section 2, the background and motivation are provided. Details of the proposed design methodology of IDGSA-3M are presented in Section 3. In Section 4, the application of IDGSA-3M to the GSA of the thermal design parameters for an ultraviolet radiation detector is described and the results are compared with those of two classical GSA methods. Finally, in Section 5 and 6, the discussion and conclusions of this study, respectively, are presented.

2. Background and motivation

2.1. MF metamodel

Many MF metamodel methods based on scale functions [52–54] exist, among which the additive scale method has been widely studied [54]. The methods adopted in this study are expressed as

$$\hat{f}_{mf}(x) = \rho \hat{f}_l(x) + \hat{\delta}(x), \tag{1}$$

where $\hat{f}_{mf}(x)$ denotes the MF-based metamodel, $\hat{f}_l(x)$ denotes the LF-based metamodel, ρ denotes the LF scale factor, and $\hat{\delta}(x)$ denotes the scaling function. The LF-based metamodel and scaling function are constructed using the Kriging model [55].

The metamodel $\hat{f}_l(x)$ is established from the LF sample space $x_l = \{x_{l,1}, x_{l,2}, \cdots, x_{l,m_l}\}$ and the results of the corresponding $f_l = \{f_{l,1}, f_{l,2}, \cdots, f_{l,m_l}\}$. For the given HF sample space $x_h = \{x_{h,1}, x_{h,2}, \cdots, x_{h,m_h}\}$ and the results of the corresponding $f_h = \{f_{h,1}, f_{h,2}, \cdots, f_{h,m_h}\}$, the error $\delta(x_{h,i}) = \{\delta(x_{h,1}), \delta(x_{h,2}), \cdots, \delta(x_{h,m_h})\}$ of the HF and LF metamodels at the HF sampling point $x_{h,i}$ can be calculated using

$$\delta(x_{h,i}) = f_h(x_{h,i}) - \rho \hat{f}_l(x_{h,i}). \tag{2}$$

With the HF sample space x_h and the results of the corresponding $\delta(x)$ for the scaling data, the Kriging model is used to construct the scaling function $\hat{\delta}(x)$ [56]. A widely used method for selecting the LF scale factor is minimizing the distance between the HF sample points and the LF scaled metamodel:

$$\text{find } \rho$$

$$\min e = \sum_{i=1}^{n} \left[\rho \hat{f}_l(x_{h,i}) - f_h(x_{h,i})\right]^2, \tag{3}$$

where n denotes the number of HF sampling points. However, this approach ignores the fluctuation effects of the scale function.

2.2. Density-based GSA

Density-based GSA, which does not address the output at a particular moment in time but considers the entire distribution, has been studied for a long time by Park and Ahn, Chun et al., and Borgonovo [57–59]. By definition, it takes into account the probability distribution of the output and not only the output at a certain point in time. Specifically, the sensitivity to x_i is the value measured by the distance between the unconditional probability distribution of y obtained when all inputs change simultaneously and the conditional distribution obtained when all inputs change except x_i.

For brevity, the conditional and unconditional probability distributions are characterized using their CDFs instead of PDFs because CDFs are easier to calculate [60–62]. The following time-independent GSA is defined:

$$\delta_i = \frac{1}{2} E_{X_i} \left[s\left(X_i\right) \right]. \tag{4}$$

Suppose that $F_Y(y)$ and $F_{Y|X_i}(y)$ intersect at m points of intersection, $y = a_1, a_2, \cdots, a_m$. If $F_Y(a_1) - F_{Y|X_i}(a_1) > 0$,

$$\begin{aligned} s\left(X_i\right) = 2\Big\{ & \left[F_Y\left(a_1\right) - F_{Y|X_i}\left(a_1\right)\right] - \left[F_Y\left(a_2\right) - F_{Y|X_i}\left(a_2\right)\right] + \cdots \\ & + (-1)^{(m-1)} \left[F_Y\left(a_m\right) - F_{Y|X_i}\left(a_m\right)\right]\Big\}. \end{aligned} \tag{5}$$

If $F_Y(a_1) - F_{Y|X_i}(a_1) < 0$,

$$\begin{aligned} s\left(X_i\right) = 2\Big\{ & \left[F_{Y|X_i}\left(a_1\right) - F_Y\left(a_1\right)\right] - \left[F_{Y|X_i}\left(a_2\right) - F_Y\left(a_2\right)\right] + \cdots \\ & + (-1)^{(m-1)} \left[F_{Y|X_i}\left(a_m\right) - F_Y\left(a_m\right)\right]\Big\}, \end{aligned} \tag{6}$$

$$E_{Xi}\left[s\left(X_i\right)\right] = \int F_{X_i}\left(x_i\right) s\left(X_i\right) dx_i, \tag{7}$$

where δ_i denotes the sensitivity index of input X_i to Y; $s(X_i)$ denotes the separation between the output density $F_Y(y)$ and the conditional density of Y, $F_{Y|X_l}(y)$ given X_i; and $F_{Xi}(x_i)$ denotes the density of X_i. The expectation $E_{X_i}[s(X_i)]$ accounts for the average shift in the decision-maker's view of the output provided by X_i.

3. Intelligent sensitivity analysis framework

In this section, the details of the intelligent sensitivity analysis framework are presented. First, the sampling strategies of the proposed framework are introduced. The batch processing system based on the MF metamodel is then described. Next, to further accelerate the evaluation of the model, the RBF neural network based on an IMEA is specified. Finally, a practical workflow is presented in detail.

3.1. Sample input spaces

Before GSA can be evaluated, it is necessary to first select an appropriate sampling strategy to sample the inputs within their variability space that can be used to construct a sample input space.

Many efficient sampling strategies exist, for example, Latin hypercube sampling (LHS), which is a statistical method for generating random samples of approximate parameter values in the multivariate that has long been widely applied in the GSA of multiple parameters [63–65]. However, a common drawback of traditional LHS and many other widely used sampling strategies is that they generate the entire sampling space at once, which requires the user to specify the sample size before sampling. Generally, users tend to use large sample sizes, although this may increase the number of unnecessary calculations and even lead to oversampling. However, when sample-based analysis fails to meet users' needs (e.g., the sample size needs to be expanded), the expanded samples should be used for sample-based analysis. At this point, users encounter a difficult problem. The expanded samples and previous samples cannot form a complete Latin hypercube; hence, the original samples are discarded and the expanded samples are recalculated, which increases the computation costs significantly.

To solve these problems, a novel efficient sequential version of the LHS proposed by Razi [66] was applied in this study, called progressive Latin hypercube sampling (PLHS). PLHS is an algorithm that uses sampling in stages. The sample sets at each stage are obtained using LHS; hence, the sample sets at all stages are Latin hypercubes, that is, PLHS allows users to observe the effect of sample-based analysis and terminate sampling based on actual demand. This not only avoids the impact of model parameter uncertainty on the sampling space as well as on the GSA, but also ensures that the sampling space is homogeneous and representative of the overall distribution of the model parameters, which greatly improves the efficiency of sampling and model evaluation. A mathematical scheme of PLHS follows.

Suppose $S(n, p)$ is a sample matrix consisting of $n \times p$ variables $x_{i,j} \in [0, 1]$, where $i = 1, \ldots, n$ and $j = 1, \ldots, p$. Additionally, a new set of auxiliary binary variables, $y_{q,j}$, is defined:

$$y_{q,j} = \begin{cases} 1 \\ 0 \end{cases} \tag{8}$$

$$\frac{\sum_{j=1}^{p} \sum_{q=1}^{n} y_{q,j}}{n.p} = 1. \tag{9}$$

When Eq. (9) is satisfied, $S(n, p)$ is a sample space based on LHS and can be referred to as LHS sampling at this stage:

$$\sum_{t=1}^{T} \frac{\sum_{j=1}^{p} \sum_{q=1}^{n_t} y_{q,j}^{t}}{n_t.p} = T, \tag{10}$$

where $t = 1, 2, \ldots, T$ is the number of stages. In essence, determining the solution of PLHS is regarded as an optimization problem:

$$\text{Maximize} \left(\sum_{t=1}^{T} \frac{\sum_{j=1}^{p} \sum_{q=1}^{n_t} y_{q,j}^{t}}{n_t.p} \right). \tag{11}$$

3.2. Batch processing system based on an MF metamodel

After establishing the sample input space, the model is then evaluated with inputs from the space. In traditional thermal analyses of spacecraft, a large amount of data for the thermal design parameters and thermophysical model parameters need to be loaded. Manually loading data into software such as NX/TMG and extracting thermal analysis results are the most widely used approaches, but are nonetheless time-consuming and error prone.

An intelligent batch processing system based on machine learning and an MF metamodel is proposed in this paper. The MF metamodel not only speeds up model estimation but also ensures the accuracy of model estimation. The intelligent batch processing system incorporates the automation of data loading and extraction of thermal analysis results. The two methods proposed in this section not only improve the speed of model estimation, but also ensure its accuracy.

The intelligent batch system consists of multiple functional modules (Fig. 1), including the (i) Software Interface module for communication between modules; (ii) Input Samples module, which generates multiple sets of thermal design parameters for the spacecraft using PLHS; (iii) Text Retrieval module, which applies the macro-recording function of FEA software to record the process of space thermal analysis based on machine learning for analysis and learning, and generates a text file that can be recognized and run by FEA software; (iv) Parameter Extraction module, which transfers the sampling data from the Input Samples module to a text file from the Text Retrieval module; and (v) Thermal

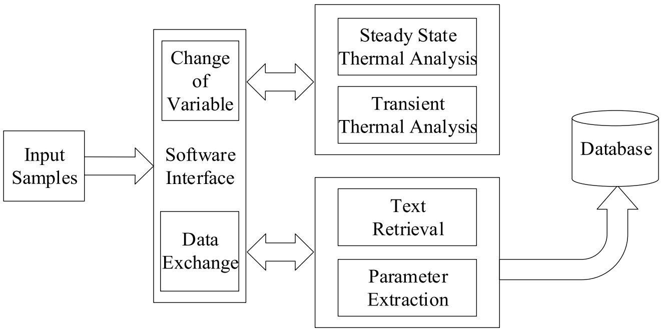

Fig. 1. Workflow of the batch processing system.

Analysis module, which performs transient thermal analysis and steady-state thermal analysis on MF metamodel, and serves to run specified space thermal analysis programs in FEA software (e.g., NX/TMG) based on the text file produced by the Text Retrieval module. The results of the calculation and the analysis change the variables, and data exchanges are performed in real time through the Software Interface module. After the resulting data are processed by the Text Retrieval and Parameter Extraction modules, which execute machine learning algorithms, it is automatically aggregated into a database as needed for later GSA.

The intelligent system implements a sampling of thermal design parameters, parameter loading, and extraction of the space thermal analysis results. Additionally, it automates the construction of datasets of the space thermal analysis results under unsupervised, which not only effectively saves manpower and reduces time consumption, but also significantly improves the efficiency of space thermal analysis.

3.3. RBF neural network based on an IMEA

Designed by Powell in 1987 [67], the RBF neural network is a widely applied multilayer feedforward neural network, which has a simple structure, concise training, and fast learning convergence, and approximates any nonlinear function. The IMEA is an evolutionary algorithm that was proposed by Yanqing et al. in 2018 [51]; it contains an optimization algorithm for the mind evolutionary algorithm proposed by Chengyi et al. [68]. Its RBF is a Gaussian function, for which its activation function is

$$r\left(x_q - c_i\right) = \exp\left(-\frac{1}{2\sigma_r^2}\left\|x_q - c_i\right\|^2\right), \tag{12}$$

and the output of the network is

$$y_j = \sum_{i=1}^{k} \omega_{ij} \cdot \exp\left(-\frac{1}{2\sigma_r^2}\left\|x_q - c_i\right\|^2\right),\ j = 1, 2, \cdots, n, \tag{13}$$

where x_q denotes the q^{th} input vector of the n dimensional vector x, c_i denotes the center of the Gaussian function, and ω_{ij} denotes the connection weight between the hidden and input layers.

The proposed RBF based on an IMEA (Fig. 2) incorporates the following optimization steps:

(1) Depending on the topology of the RBF, the mapping of the solution space to the coding space is achieved, and the length of IMEA coding is determined from

$$L = L_1 L_2 + L_2 L_2 + L_2 L_3 + L_2 + L_3 \tag{14}$$

where L_1, L_2, and L_3 are the number of nodes in the input layer, hidden layer, and output layer, respectively.

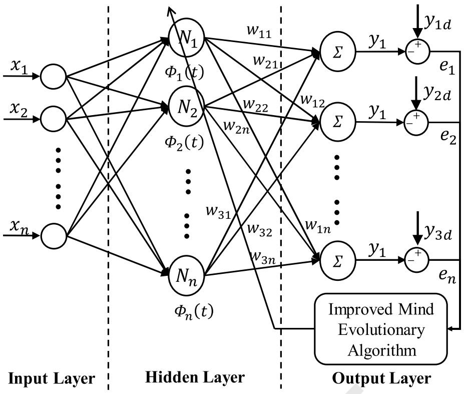

Fig. 2. Structure of the RBF neural network based on an IMEA.

(2) The reciprocal of the MSE of the training set is selected as the reward function F of each individual and population, and expressed as

$$F = \frac{n}{\sum_{i=1}^{n}\left(x_{obs,i} - x_{pre,i}\right)^2}, \tag{15}$$

where $x_{obs,i}$ is the true value of the i^{th} sample and $x_{pre,i}$ is the predicted value of the i^{th} sample.

(3) The group is initialized to obtain an excellent subgroup and a temporary subgroup. After convergence and mutation operations, the global optimal individual and its score are obtained.

(4) The optimal parameters obtained from the RBF optimized by the IMEA are input into the RBF for further training.

3.4. Practical workflow of IDGSA-3M

The proposed IDGSA-3M is divided into two stages and seven steps, and applies three programming languages and space thermal analysis software to take advantage of each programming language and analysis software (Fig. 3).

The 1$^{\text{st}}$ stage: First, LF metamodels are applied to enhance the computational efficiency of the sensitivity analysis while maintaining the accuracy of the model output through HF metamodels. Then, an RBF neural network based on an IMEA (RBF-IMEA) is applied to approximate the thermophysical model of the spacecraft calculated by the batch MF system and subsequently used as the function for later GSA to accelerate post-processing. Finally, the effect of RBF-IMEA is evaluated and a determination is made on whether to further expand the sampling space based on the convergence analysis.

The 2$^{\text{nd}}$ stage: First, the sampling space based on PLHS for GSA is generated. Then, the model is evaluated by the Batch-RBF system based on RBF-IMEA generated in the 1$^{\text{st}}$ stage. Finally, the effect of the density-density GSA is evaluated depending on the convergence analysis, and again, a determination is made on whether to further extend the sampling space.

After these two steps, the results are graphed to enable a comparative analysis of GSA. The key is that all the above steps are performed automatically without human supervision. Both the computational efficiency of the GSA and the accuracy of model evaluation are improved.

4. Example applications and results

To verify its performance, IDGSA-3M is applied to the GSA for the thermal design parameters of a detector for extreme ultraviolet (EUV) radiation situated on the space-based Lyman-alpha

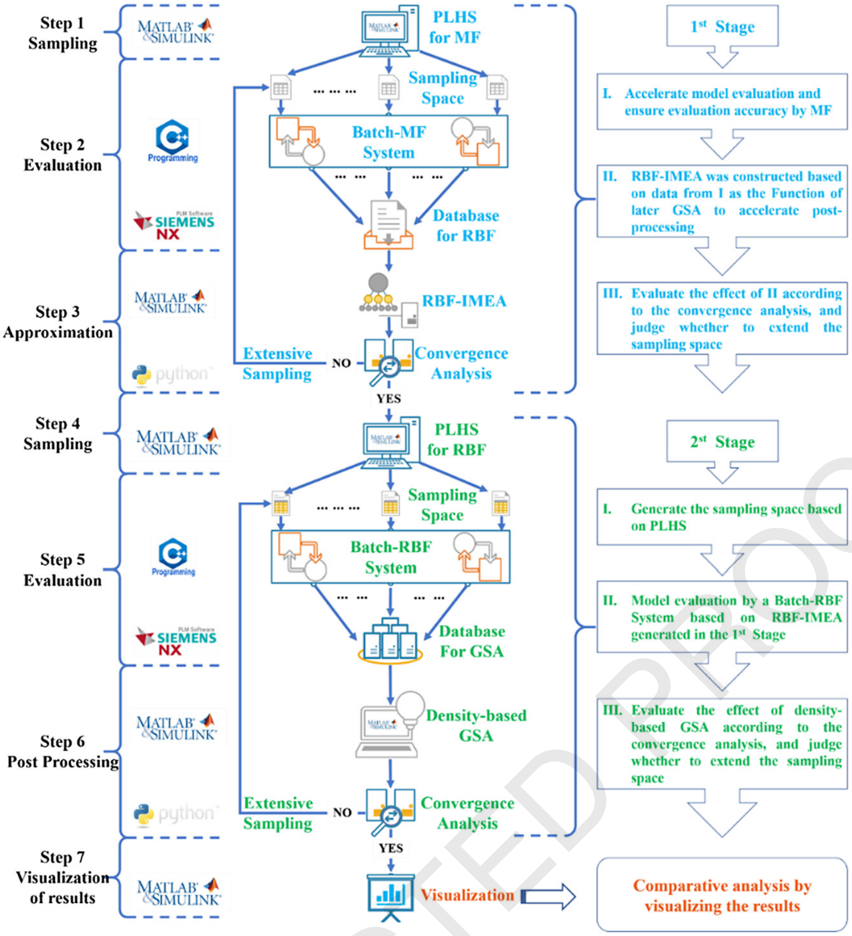

Fig. 3. Practical workflow for IDGSA-3M.

Solar Telescope (LST) developed by China, and compared with MFGSA, PAWN, and the traditional method based on the Monte Carlo method and manual tuning.

In this section, the application of IDGSA-3M to the LST is described in detail. First, the research background of the LST is introduced. Then the thermophysical model of the LST is described. Next, based on the proposed IDGSA-3M, sensitivity analysis of thermal design parameters of the LST is conducted under high temperature conditions. Finally, IDGSA-3M is compared with the classical density-based PAWN method and the classical Monte Carlo-based and manually adjustable MFGSA method.

4.1. Background of the LST

To meet the needs of astronomers for the observation and study of various solar activities, such as coronal mass ejections, solar flares, and sunspots, the Chinese Academy of Sciences designed a new space-based Lyman alpha and visible dual-band internal occulting coronagraph that enables simultaneous high-resolution imaging and observation of the corona at 121.6 nm and 700 nm. The overall structure of the LST is shown in Fig. 4A. The lens barrel always faces the sun. The SCI121.6 detector and SCI700 detector are the two core detectors of the LST, which are the basic equipment for observing solar activity in 121.6 nm and 700 nm bands, and studying solar internal dynamics, respectively. However, the cold black space, sharp transition between high and low temperatures, single particle effect, atomic oxygen corrosion, and other space environmental factors have significant effects on the observation. As shown in Table 1, the parameters and settings of the orbital environment are described, which indicates that the LST operates in a solar synchronous orbit at 720 km altitude and faces a complex thermal environment, including direct sunlight, infrared radiation from the Earth, and reflected sunlight from the Earth (see Fig. 5). Additionally, there is a large difference in heat flux between the sunny side and the shady side, which may lead to an uneven temperature distribution between the main mirror and detectors, thus affecting the imaging quality of the LST. Therefore, it is necessary to design a reliable, effective, and accurate thermal control system for the LST, particularly for the detector.

Table 1
Parameters and settings for the orbital environment.

Parameter	Hot case	Cold case
Orbit	Sun-synchronized orbit	
Minimum Altitude	720 km	
Spacecraft Attitude	Lens barrel is facing the sun and orbiting under inertia	
Satellite Position	Local Time at Ascending Node 18:00:00	
Orbit Period	5942.6 s	
Orbit Inclination	98.38°	
Albedo	0.306	
CMOS Power	0.65 W	
System Heating Power	≤120 W	
Temperature Index for Frameworks	19∼25 °C	
Stefan-Boltzmann Constant	5.67×10^{-8} W/(m^2· K^4)	
Solar Constant	1412 W/m^2	1322 W/m^2
Earth IR	237 W/m^2	220 W/m^2

Because of the complex and changeable space environment, the LST requires very high thermal control accuracy during storage and operation. The operating temperature range of the frame is 19 °C–5 °C. The SCI121.6 detector is required to maintain a low op-

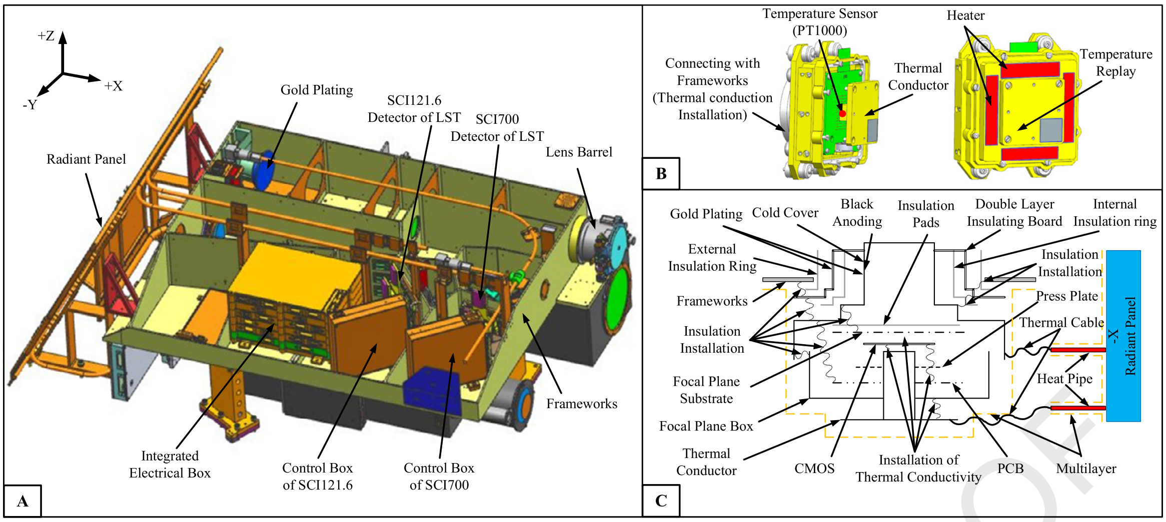

Fig. 4. Overall structure of the LST and detector. (A) Overall structure of the LST. (B) Heaters attached to the SCI121.6 detector. (C) Structure diagram of the SCI121.6 detector.

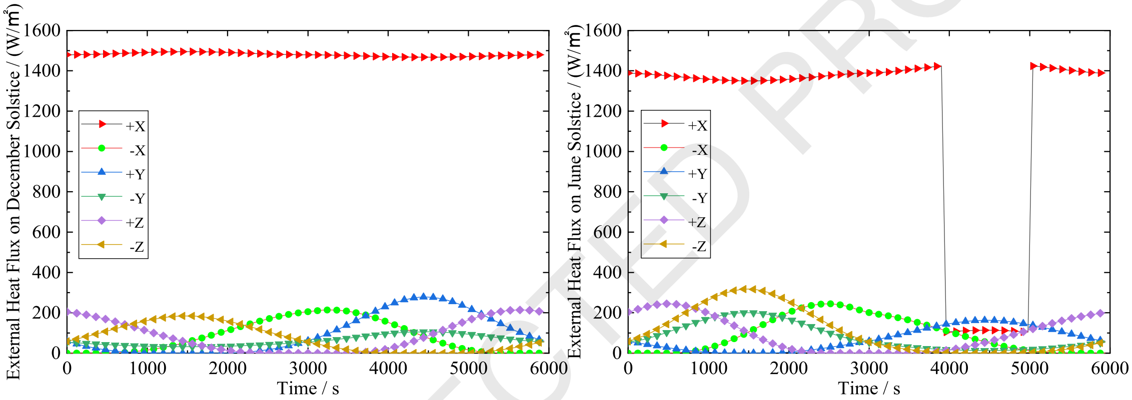

Fig. 5. External heat flux of the LST in the hot case and cold case.

Table 2
List of materials used in the detector and their physical properties.

Name	Material	Density Kg/m^3	Thermal conductivity W/m·K	Specific heat capacity J/kg·K
Focal plane box	Aluminum alloy (2A12)	2780	121	921
CMOS	Photosensitive material	1800	20	500
PCB	Composite materials	1800	20	500
Thermal conductor	Aluminum alloy (7A09)	2850	134	921
Thermal cable	Copper	8750	350	400
Cold cover	Aluminum alloy (7A09)	2850	134	921
Insulation pads/rings	Polyimide	1420	0.25	1130

erating temperature of −50 °C to −20 °C. Because the CMOS in the SCI121.6 detector relies on an aluminum ammonia heat pipe for cooling (see Fig. 4C), and this pipe will fail when it is lower than −70 °C, the temperature of the CMOS must be controlled at −30 °C to −25 °C, which poses a great challenge to the thermal design of the SCI121.6 detector. Fig. 4C shows the structure diagram of the SCI121.6 detector after careful thermal design. Table 2 details the materials used in the detector and their physical characteristics, which are also affected by manufacturing and craftsmanship (see Table 3). In particular, the optimization of a large number of thermal design parameters would be very time-consuming and almost impossible if it was based on the thermal design engineer's experience.

Table 3
List of surface craft and their thermophysical properties.

Name	Solar absorptivity	Infrared emissivity
Black anodizing	0.80-0.95	0.80-0.95
Gold plating	0.15-0.40	0.02-0.05
S781 white coatings	0.12-0.25	0.80-0.94
F46	0.11-0.45	0.60-0.80

The sensitivity analysis of the thermal design parameters of the LST is very important for the thermal design of the LST. Sensitivity analysis generally focuses on two types: local sensitivity analysis (LSA) and GSA. LSA examines the change in the response of the temperature of the LST caused by a small variation in a single model parameter. However, LSA does not provide global information about the impact of parameter uncertainty. GSA addresses the limitations of the LSA, which is one advantage of the proposed IDGSA-3M. In the context of model-based design, GSA can guide research aimed at reducing model parameter uncertainties that significantly affect the expected performance and allow engineers to neglect model parameters that do not significantly affect the temperature of the LST. To verify the performance of IDGSA-3M, it was applied to the GSA of thermal design parameters affecting the CMOS temperature of the EUV radiation detector on the space-based LST, which is called the SCI121.6 detector. Fig. 4C shows the structure of the SCI121.6 detector.

4.2. Thermophysical model of the LST

4.2.1. Theoretical analysis of the thermophysical model

Before IDGSA-3M can be applied to the thermal analysis of the LST, the thermophysical model of the spacecraft needs to be analyzed. Currently, the node network method [69,70] is the most commonly used method in modeling spacecraft thermal design. Depending on their characteristics, the LST can be broken into numerous finite units, each of which is treated as an isothermal object. The application of the heat balance equation for each node yields

$$Q_{sj} + Q_{pj} + \sum_{i=1}^{M} B_{i,j} A_i \varepsilon_i \sigma T_i^4 + \sum_{i=1}^{N} D_{i,j}(T_j - T_i) = (cm)_j \frac{dT_j}{d\tau} + A_j \varepsilon_j \sigma T_j^4, \quad (16)$$

where Q_{sj} is the external heat flux absorbed by node j; Q_{pj} is the internal thermal power consumption of node j; $B_{i,j}$ is the Gebhart factor; A_i is the radiant heat transfer area of node i facing node j; ε_i is the infrared emissivity of node i facing node j; σ is the Stefan–Boltzmann constant; T_i denotes the real-time temperature value for node i; M is the number of nodes that exchange radiant heat with node j; $D_{i,j}$ is the thermal conductivity coefficient between node i and node j; T_j denotes the real-time temperature value for node j; N is the number of nodes that exchange conduction heat with node j; $(cm)_j$ is the heat capacity of node j; c is the specific heat capacity of node j; m is the quality of node j; τ is time; A_j is the area of radiant heat dissipation of node j; and ε_j is the infrared emissivity of node j for radiant heat dissipation. For each node on the spacecraft, such an equation can be derived, and the temperature of each node can be obtained using a simultaneous solution, which is called the node network method:

$$(cm)_j \frac{dT}{d\tau} = \sum_i R_{i,j}(T_j^4 - T_i^4) + \sum_i D_{(i,j)}(T_j - T_i) + Q_{sj} + Q_{pj}, \quad (17)$$

where $R_{(i,j)}$ is the heat transfer coefficient of the heat radiation network between nodes in the network mode and $D_{(i,j)}$ is the thermal conductivity coefficient of the heat conduction network between nodes in the network model.

4.2.2. Boundary conditions

The common boundary conditions in space thermal analysis can be classified into three categories:

(I) the temperature at the boundary of the spacecraft at any time:

$$\tau > 0, \quad T_w = f_T(x, y, z, \tau), \quad (18)$$

where T_w is the temperature of the boundary of the spacecraft; f_T is a function of the temperature at the boundary of the spacecraft; and (x, y, z) denotes the coordinates of the spacecraft boundary in the space coordinate system;

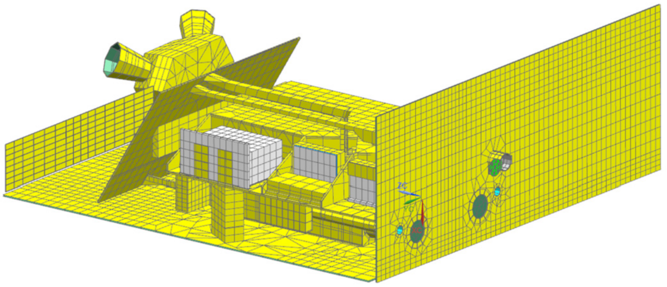

Fig. 6. Thermophysical model of the LST.

(II) the heat flux on the boundary at any time:

$$q_w = f_{hl}(x, y, z, \tau), \quad (19)$$

where q_w is the heat flux in the normal direction on the spacecraft boundary and f_{hl} is a function of the heat flux at the boundary of the spacecraft; and

(III) the temperature and convective heat transfer coefficient of the fluid medium conducting with the spacecraft:

$$\left.\frac{\partial T}{\partial n}\right|_w = -\frac{h}{\lambda}(T_w - T_f), \quad (20)$$

where $\left.\frac{\partial T}{\partial n}\right|_w$ is the temperature gradient in the normal direction on the spacecraft boundary; h is the convective heat transfer coefficient between the spacecraft surface and fluid; λ is the thermal conductivity coefficient of the material; and T_f is the temperature of the fluid medium conducting with the spacecraft.

4.2.3. Establishing the thermophysical model of the LST

According to the three-dimensional model of the LST and the thermal control scheme, the thermal physical model of the LST was established using NX/TMG, as shown in Fig. 6. The model has 53,970 cells, 55,874 nodes, and 236 thermal couplings.

4.3. Application of IDGSA-3M

4.3.1. Sample input spaces based on PLHS

Before the proposed IDGSA-3M is used to conduct GSA of the key thermal design parameters of the SCI121.6 detector, a sampling space needs to be constructed. Convection is not considered in this study because it is only relevant for pressurized spacecraft with an internal atmosphere. When selecting the thermal design parameters for GSA, the first selection criterion is based on whether the parameters in the SCI121.6 detector can be arbitrarily changed as the selection criteria. Because of the limitation of the optical structure of the system, many parameters that affect the temperature T cannot be changed. Then, among the parameters that can be changed, the main parameters that are directly or indirectly related to the temperature T are selected:

(a) For the selection of adjustable parameters that directly affect the temperature T of the CMOS, the parameters related to direct thermal radiation and conduction by the CMOS are mainly selected because of the vacuum treatment in the detector. In terms of the selection of the radiation parameters, because the inner surface of the focal plane box and the thermal conductor transfer radiation heat to the CMOS, they are mainly selected. In terms of the selection of the heat conduction parameters, as the thermal conductor, press plate, and focal plane box are directly connected with the CMOS thermally, they must be selected. Thermal resistance is related to the contact surface and thermal conductivity, and the radiation parameters are related

Table 4
Descriptions and ranges of the thermal design parameters.

	Parameter number	Description	Base value	Lower limit	Upper limit
Solar absorptivity	1	Inner surface of the cold cover	0.84	0.80	0.95
	2	Outer surface of the cold cover	0.25	0.15	0.40
	3	Radiation panel	0.18	0.12	0.25
	4	Inner surface of double layer insulating board	0.84	0.80	0.95
	5	Outer surface of double layer insulating board	0.25	0.15	0.40
	6	Inner surface of focal plane box	0.84	0.80	0.95
	7	F46	0.41	0.11	0.45
Infrared emissivity	8	Inner surface of the cold cover	0.84	0.80	0.95
	9	Outer surface of the cold cover	0.05	0.02	0.05
	10	Radiation panel	0.87	0.80	0.94
	11	Inner surface of double layer insulating board	0.84	0.80	0.95
	12	Outer surface of double layer insulating board	0.05	0.02	0.05
	13	Inner surface of focal plane box	0.84	0.80	0.95
	14	F46	0.68	0.60	0.80
Thermal resistance, $K \cdot W^{-1}$	15	Between thermal cable and thermal conductor	1.11	0.13	2.5
	16	Between thermal cable and cold cover	0.23	0.13	2.5
	17	Between thermal cable and heat pipe	1.23	0.13	2.5
	18	Between heat pipe and thermal cable	0.67	0.13	2.5
	19	Between thermal conductor and CMOS	4.22	1.48	4.44
	20	Between thermal conductor and focal plane box	1.18	0.71	3.53
	21	Between cold cover and insulation pads	3.79	2.28	25
	22	Between cold cover and PCB	201.81	21.4	273.14
	23	Between cold cover and double layer insulating board	68.42	3.98	81.68
	24	Between cold cover and focal plane box	11.74	1.86	38.01
	25	Between double layer insulating board and framework	68.42	3.98	81.68
	26	Between double layer insulating board and external insulation ring	5.00	0.63	10
	27	Between double layer insulating board and internal insulation ring	5.00	0.47	10
	28	Between external insulation ring and framework	15.00	2.5	25
	29	Between internal insulation ring and cold cover	5.00	2.10	10.47
	30	Between focal plane box and CMOS	6.93	4.16	40
	31	Between focal plane box and insulation pads	3.79	2.28	40
	32	Between focal plane box and press plate	3.89	2.34	40
	33	Between CMOS and press plate	12.15	7.29	66.67
	34	Between CMOS and PCB	4.47	2.68	13.42
Thickness, mm	35	Internal insulation ring	2.35	1	5
	36	External insulation ring	2.91	1	5
	37	Insulation pads	1.24	1	5
Heat transfer coefficient, $W \cdot m^{-2} \cdot K^{-1}$	38	Between multilayer and wrapped area	0.17	0.05	0.6
Thermal conductivity, $W \cdot m^{-1} \cdot K^{-1}$	39	Thermal conductor	154.00	100	250
	40	Thermal cable	300.00	150	300
	41	Cold cover	154.00	100	250
	42	Focal plane box	154.00	100	250

to the surface craft and material properties. The value ranges of the selected radiation parameters and thermal resistance are shown in Table 4. Additionally, the thermal conductivity of the thermal conductor also has a direct impact on the CMOS temperature, and its value also depends on the surface craft and material properties.

(b) For the selection of parameters that indirectly affect the temperature T of the CMOS, the parameters that affect the temperature of the cold cover and focal plane box are mainly selected. Because the radiation parameters of the inner and outer surfaces of the cold cover and double layer insulating board both affect the temperature of the focal plane box through heat conduction, they must be selected. The components that are directly or indirectly connected to the cold cover and focal plane, such as PCB, insulation pads, and the press plate, have an indirect effect on the CMOS temperature, so they must be selected. Additionally, the thickness of the insulation ring and insulation pads also has an indirect effect on the CMOS temperature through heat conduction. Simultaneously, the heat transfer coefficient between the multilayer and wrapped area directly affects the temperature of the focal plane box through radiant heat transfer, so they must be selected. The value ranges of the selected parameters are shown in Table 4.

To establish RBF-IMEA with 42 thermal design parameters as input and COMS temperature T as output, the training set should be established. First, 42 parameters need to be sampled in their respective value spaces. To avoid the inhomogeneity of the sampling input space, that is, the whole value space of the parameters cannot be covered, which leads to the great error of the prediction of RBF-IMEA, the PLHS method is adopted in this study to sample 42 parameters in their value space, which can effectively improve the coverage of the sample values on the distribution space of the input random variables and avoid the impact of the uncertainty of the model parameters on the sampling space, finally forming a sample input space composed of 5,000 sets of data.

4.3.2. Reduction of the space thermal mathematical models

In the thermal analysis of spacecraft, thermal radiation is the main heat transfer mechanism, and the Monte Carlo Ray Tracing (MCRT) method [71] is the most widely used method to solve it. However, the MCRT method essentially requires a long computational time and a large number of computational resources. Therefore, to improve the efficiency of thermal analysis, thermal

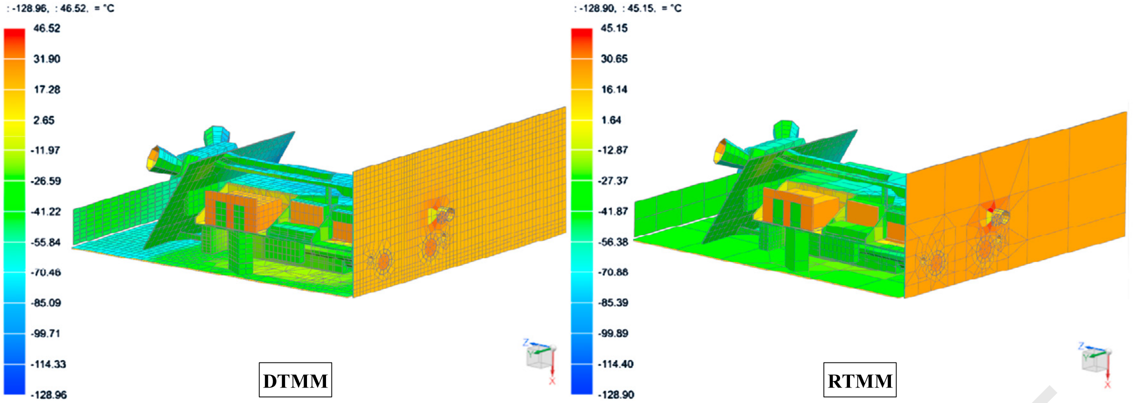

Fig. 7. Thermal analysis results of the DTMM and RTMM under the hot case based on the base value. (For interpretation of the colors in the figure(s), the reader is referred to the web version of this article.)

Table 5
Settings for six sample size combinations.

	RTMM sample size	DTMM sample size	MSE
Case 1	2500	2500	15.6836
Case 2	3000	2000	3.4361
Case 3	3500	1500	1.2871
Case 4	3750	1250	0.9596
Case 5	4000	1000	4.3568
Case 6	4500	500	16.5249

model reduction is widely used. In this study, the thermal model reduction strategy proposed by Michael [72] is adopted. Based on this method, the detailed thermal mathematical model (DTMM) of the LST is used to obtain the reduced thermal mathematical model (RTMM) using reduction correlation, and then the Kriging model is established for the scaling function and RTMM metamodel.

In this study, the RTMM with 13,977 cells and 14,900 nodes is regarded as an LF metamodel, whereas the DTMM with 53,970 cells and 55,874 nodes is considered as an HF metamodel. The time taken for modeling and simulation of an HF metamodel is about three times that for an LF metamodel. Using the base values in Table 4, the DTMM and RTMM were simulated for 10 orbital periods under the hot case, and the temperature distribution of the CMOS was calculated when the temperature was stable. As shown in Fig. 7 the temperature difference between the DTMM and RTMM was less than 2 K, which is accepted in the initial thermal design of the LST.

4.3.3. Batch processing based on the MF metamodel

The sample input space composition of 5,000 sets of data was transferred to the batch processing system proposed in this paper, then the intelligent automatic thermal analysis of the DTMM and RTMM of the LST was conducted without manual operation. After the thermal analysis, the approach used to match the DTMM and RTMM to construct the MF metamodel was analyzed. From the effect of the RTMM/DTMM and their corresponding coefficients on each other (Table 5), the MSE of the resulting model was smallest when 3,750 RTMM models and 1,250 DTMM models were used to construct the MF metamodels.

4.3.4. RBF neural network based on an IMEA

In this study, to obtain the RBF neural network surrogate model with high fitting accuracy and improve the training and convergence speed of the model, the RBF neural network toolbox of MATLAB was used. In the training process, 80% of the original samples in the dataset of 50,000 evaluation data sets obtained by MF metamodels were used for training, 10% were used to validate the generality of the network, and the remaining 10% were used for testing. After RBF neural network surrogate model was trained for 695 iterations, its MSE was 5.489e-2, which was greater than the preset training goal of 1e-3 and did not satisfy the convergence requirement. The regression analysis in Fig. 8 shows that the computational error between the RBF neural network surrogate model and the traditional thermophysical model is still less than 85%, so the hyperparameters of the RBF neural network surrogate model must be optimized.

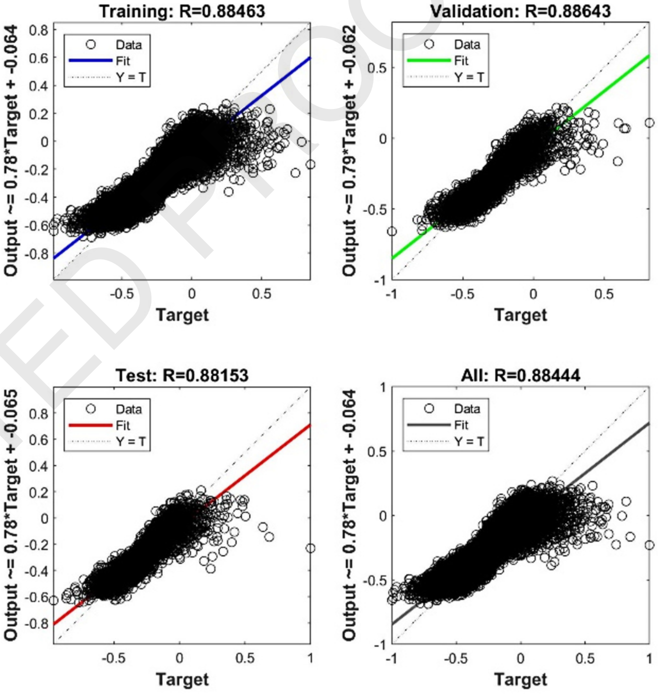

Fig. 8. Regression of the established RBF neural network surrogate model without optimization.

As described in subsection 3.3, IMEA is used to optimize the hyperparameters of the RBF neural network surrogate model in this study. Finally, after 244 iterations of training and optimization, an RBF neural network surrogate model with a structure of 42-168-84-40-4-1 was obtained, and its mean square error was reduced to 4.898e-4. Its regression analysis is shown in Fig. 9. In addition, the RBF-IMEA surrogate model has a computational speed that was 1000+ times faster than that of the traditional thermophysical model and a high computational accuracy of 99%+.

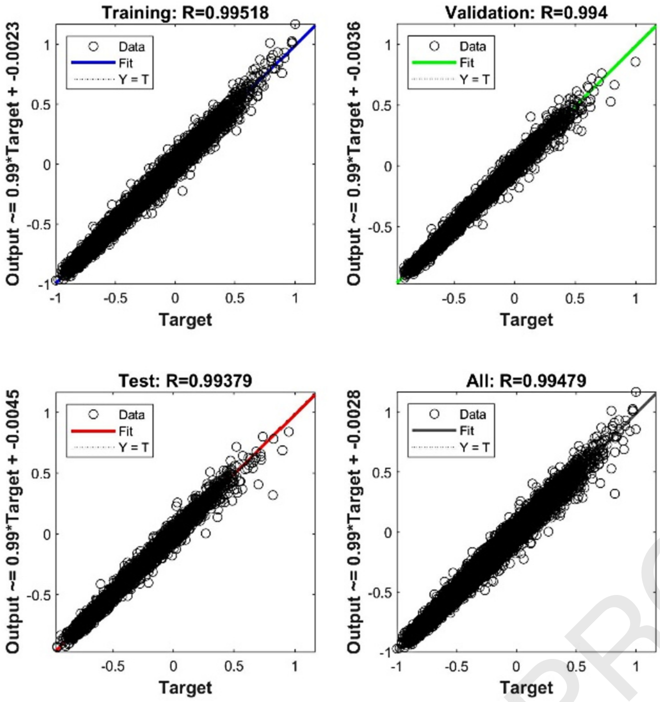

Fig. 9. Regression of the established RBF-IMEA neural network surrogate model.

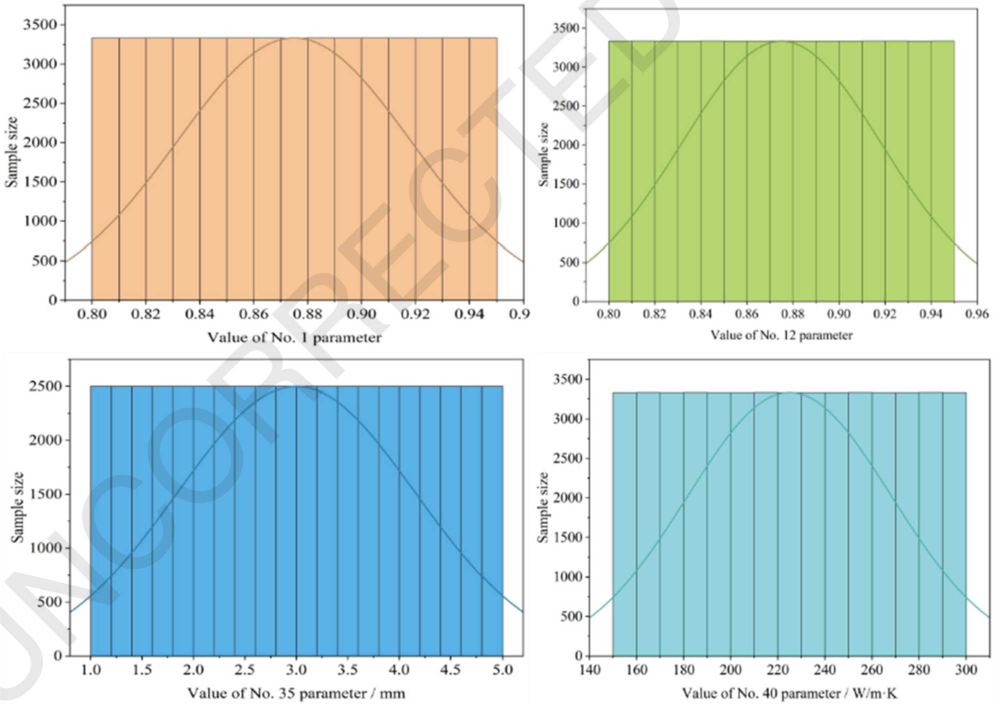

Fig. 10. Distribution of some parameters' sampling.

4.3.5. *Batch processing based on RBF-IMEA*

As mentioned earlier, the PLHS method was adopted to sample 42 parameters in their value space, which formed a sample input space composed of 50,000 sets of data. Fig. 10 shows the distribution of some parameters after 50,000 times of sampling using PLHS method, and the distribution law of other parameters not given in Fig. 10 is consistent with that of parameters in the figure. Additionally, the sample input space composition of 50,000 sets of data was transferred to the batch processing system proposed in this paper, then the intelligent automatic thermal analysis of RBF-IMEA of the LST was performed without manual operation. After the thermal analysis, 50,000 groups of sample input space and corresponding thermal analysis results constituted the dataset of the later density-based GSA.

4.3.6. *GSA of the SCI121.6 detector based on IDGSA-3M*

After RBF-IMEA achieved the desired accuracy (the absolute error of TMG-simulated T and RBF-IMEA predicted T did not exceed 0.1 K and the relative error did not exceed 0.2%), it entered the second stage (see Section 3.4). As shown in Table 6, when the

Table 6
GSA of the SCI121.6 detector based on IDGSA-3M.

	Main effect			Total effect		
No.	Median	Max	Min	Median	Max	Min
1	−0.0215	0.0063	−0.0287	0.0672	0.0736	0.0633
2	−0.0001	0.0166	−0.0048	0.0581	0.0654	0.0502
3	−0.0104	0.0123	−0.0228	0.0435	0.0482	0.0353
4	0.0870	0.1052	0.0661	0.1457	0.1507	0.1400
5	0.0582	0.0898	0.0536	0.1264	0.1324	0.1188
6	0.0022	0.0215	−0.0096	0.0610	0.0678	0.0572
7	−0.0722	−0.0486	−0.0869	0.1715	0.1865	0.1527
8	0.0093	0.0125	−0.0109	0.0886	0.0946	0.0818
9	0.0268	0.0402	0.0178	0.0993	0.1051	0.0930
10	0.0951	0.1195	0.0809	0.1635	0.1687	0.1573
11	−0.0365	−0.0208	−0.0536	0.0418	0.0476	0.0357
12	−0.0548	−0.0374	−0.0703	0.0134	0.0209	0.0078
13	−0.0241	0.0042	−0.0298	0.0382	0.0435	0.0301
14	0.0732	0.0904	0.0602	0.1366	0.1420	0.1289
15	−0.0359	−0.0082	−0.0472	0.0215	0.0262	0.0131
16	−0.0149	0.0049	−0.0285	0.0327	0.0379	0.0249
17	0.0010	0.0207	−0.0184	0.0528	0.0570	0.0439
18	0.0561	0.0800	0.0486	0.1189	0.1252	0.1146
19	**0.7908**	**0.8162**	**0.7971**	**0.8654**	**0.8774**	**0.8618**
20	0.0350	0.0625	0.0293	0.0938	0.0991	0.0865
21	0.0353	0.0600	0.0261	0.0940	0.0991	0.0874
22	0.0033	0.0275	−0.0095	0.0658	0.0711	0.0585
23	**0.4026**	**0.4289**	**0.3908**	**0.6313**	**0.6523**	**0.6178**
24	0.0921	0.1174	0.0863	0.1509	0.1562	0.1449
25	0.0916	0.1147	0.0849	0.1604	0.1655	0.1531
26	0.0470	0.0667	0.0379	0.1157	0.1216	0.1091
27	0.0813	0.1015	0.0785	0.1577	0.1624	0.1503
28	0.0837	0.1037	0.0750	0.1477	0.1531	0.1406
29	0.0663	0.0957	0.0656	0.1210	0.1268	0.1143
30	−0.0259	0.0043	−0.0254	0.0453	0.0497	0.0372
31	0.0404	0.0614	0.0324	0.1078	0.1142	0.1027
32	0.0110	0.0364	0.0053	0.0786	0.0839	0.0712
33	0.0608	0.0910	0.0572	0.1232	0.1285	0.1161
34	**0.1187**	**0.1403**	**0.1101**	**0.3375**	**0.3574**	**0.3258**
35	−0.0779	−0.0599	−0.0901	0.0191	0.0252	0.0139
36	−0.0619	−0.0452	−0.0741	0.0069	0.0110	−0.0012
37	−0.0069	0.0110	−0.0195	0.0614	0.0655	0.0525
38	−0.1833	−0.1587	−0.1988	0.0195	0.0377	0.0026
39	−0.0296	−0.0097	−0.0430	0.0391	0.0442	0.0315
40	**0.0996**	**0.1205**	**0.0998**	**0.3184**	**0.3374**	**0.3018**
41	0.1124	0.1371	0.1095	0.1811	0.1859	0.1736
42	−0.0358	−0.0060	−0.0396	0.0406	0.0449	0.0336

calculation cost reached 5,000, the difference between the maximum value and the minimum value of the sensitivity index of the 42 groups of thermal design parameters of the SCI121.6 detector based on IDGSA-3M was no greater than 0.05, which met the accuracy requirements of the GSA of the LST thermal design in the early stage.

The main effect index represents the main effect contribution of each input factor to the variance of the output. Additionally, the total effect index accounts for the total contribution to the output variation caused by the input of its main effect plus all higher-order effects caused by interactions. Table 6 shows that the main effect and total effect indices of No. 19, No. 23, No. 34 and No. 40 parameters were the largest, they all exceeded 0.2, whereas the others were almost all lower than 0.2. This result shows that the No. 19, No. 23, No. 34 and No. 40 parameters had a greater impact on the CMOS temperature, whereas the other parameters had a relatively small impact. Among all 42 parameters, that 16 parameters had a main impact indicator that was less than 0 indicates that they had little effect on the CMOS temperature and were insensitive to the CMOS temperature.

4.4. Results

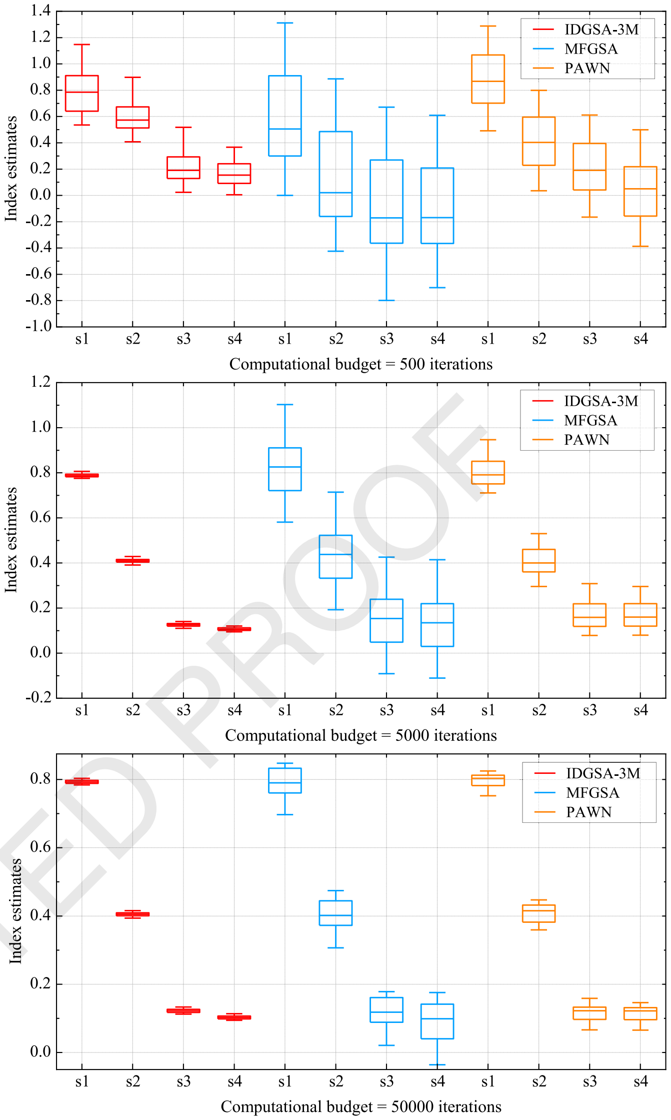

Fig. 11. Comparison of the main effect based on the three algorithms.

To compare the evaluation results obtained by MFGSA, PAWN, and IDGSA-3M, four sets of parameters with a GSA index above 0.3 were selected from Table 6 that have the greatest influence on CMOS temperature (s1: thermal resistance between the thermal conductor and CMOS; s2: thermal resistance between the cold cover and double layer insulating board; s3: thermal resistance between the CMOS and PCB; and s4: thermal conductivity of the thermal cable), and then used for analysis and comparison. Comparative analysis of the main effect (Fig. 11) and total effect (Fig. 12) of the three GSA methods was performed based on 100 sensitivity indices estimated with a computation budget of 500 iterations, 5,000 iterations, and 50,000 iterations.

Fig. 11 shows that, after IDGSA-3M had calculated the computational budget for 5,000 iterations, its main effect reached the desired accuracy (the absolute error of maximal main effect and minimal main effect for one factor did not exceed 0.1) much faster than that of MGFSA and PAWN. Indeed, neither of the latter two reached the desired accuracy when the calculation cost was 50,000 iterations. Additionally, when IDGSA-3M calculated the total effect, it also performed significantly better than the other methods (see Fig. 12). This means that IDGSA-3M was at least 10 times more efficient than the other methods.

As shown in Fig. 13, the convergence analysis of the main effect and total effect was performed based on the median, maximum and minimum values obtained by evaluating the GSA index of the

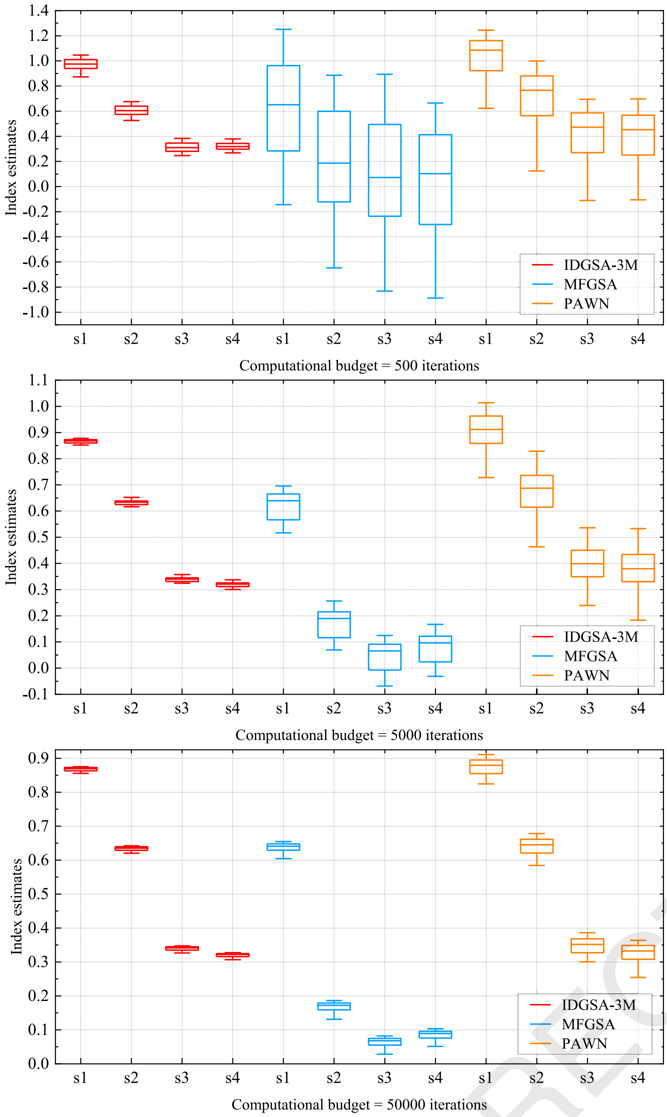

Fig. 12. Comparison of the total effect based on the three algorithms.

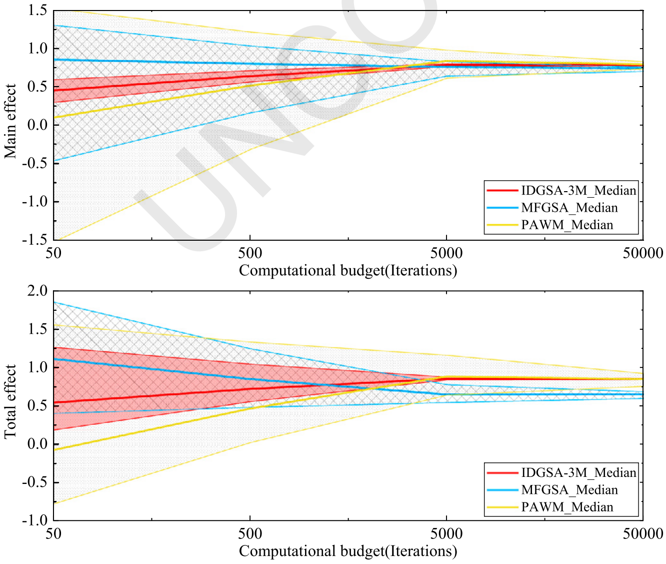

Fig. 13. Convergence analysis based on the three algorithms.

No. 19 parameter on CMOS temperature 100 times for each of the three methods at calculation budgets of 500 iterations, 5000 iterations and 50,000 iterations, respectively. Obviously, for the main effect, all three methods have almost no deviation except for the different convergence rates. For the total effect, MFGSA did not have deviations, but the convergence speed was slow. IDGSA-3M not only improved the convergence speed and model evaluation speed considerably, but also minimized deviations.

Fig. 14 shows the GSA indexes for the 10 high-impact parameters (as bolded in Table 6) calculated by the variance-based GSA MFGSA method and the density-based GSA IDGSA-3M method, along with the 95% confidence intervals estimated using 100 bootstrap resamples. In addition, which shows the results of the parameter ranking based on the GSA index. Both methods clearly show that the No. 19 parameter is the most important parameter, although the results of the parameter ranking vary, the top 5 influential parameters are similar for the MFGSA and IDGSA-3M methods. In the IDGSA-3M method, the GSA indices for parameters of rank 6 or higher are not significantly different from each other. Similarly, the MFGSA's GSA indices for parameters ranked 6 or higher are almost identical (almost zero). Therefore, this group of parameters can be considered as less influential. As shown in this Fig. 14, the IDGSA-3M method approach highlights the differences between the influencing parameters more than the MFGSA approach, for example the No. 23 and No. 25 parameters. Furthermore, as can be observed, the application of the MFGSA and IDGSA-3M methods can result in completely different GSA indices for each parameter with the reason for these differences being related to the different ranges and meanings of the indicators; the MFGSA's GSA index is based on the variance of the output, whereas the IDGSA-3M's GSA index indicates the effect of the parameter on the overall output distribution. The 95% confidence interval (red line in Fig. 1) indicates that the IDGSA-3M method has a narrower interval compared to the MFGSA method. Thus, we can conclude that the IDGSA-3M method is more robust than the variance-based GSA MFGSA method.

The computational efficiency and accuracy of the three methods (Fig. 15) were compared and analyzed with those of the traditional method based on Monte Carlo methods and manual tuning. Clearly, these traditional methods had almost no evaluation error and amplitude, whereas MFGSA and PAWN had average evaluation errors of 0.1° and 0.05 °C, and maximum evaluation error of 0.2 °C and 0.15 °C, respectively. MFGSA and PAWN took 66.7% and 33.3% less time to execute GSA based on 100 group models than the traditional method based on Monte Carlo methods and manual tuning. As a comparison, the average evaluation error and maximum evaluation error from IDGSA-3M were 0.08 °C and 0.12 °C, which were 20% and 40% greater than those of MFGSA, respectively. In terms of computation efficiency, PAWN based on the traditional Monte Carlo method takes nearly one hour for each model evaluation, and MFGSA based on the MF metamodel takes only 30 minutes, while the IDGSA-3M proposed in this study takes only 542.6 seconds for each model evaluation. Clearly the proposed IDGSA-3M was 69.86% and 84.93% faster than MFGSA and PAWN, respectively. Additionally, the calculation speed of GSA based on the MF metamodel and RBF-IMEA surrogate models in this study was also limited by the calculation resources (Intel Core i9-9900X CPU, 64 GB RAM, and GeForce RTX 2080 Ti), which resulted in a longer calculation time for the sensitivity index. Improving the computing resources will result in a further reduction of the calculation time of GSA, further promoting the application of IDGSA-3M in thermal analysis tasks.

5. Discussion

In this study, model reduction, MF metamodeling, and variance-based GSA methods were combined and used in the field of space-

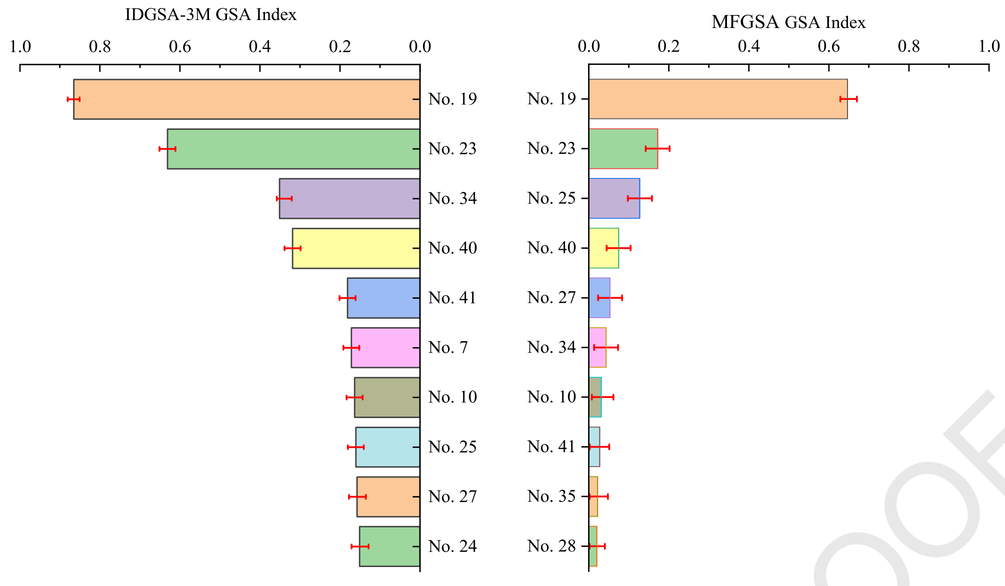

Fig. 14. IDGSA-3M (left) and MFGSA (right) GSA index of the LST model parameters.

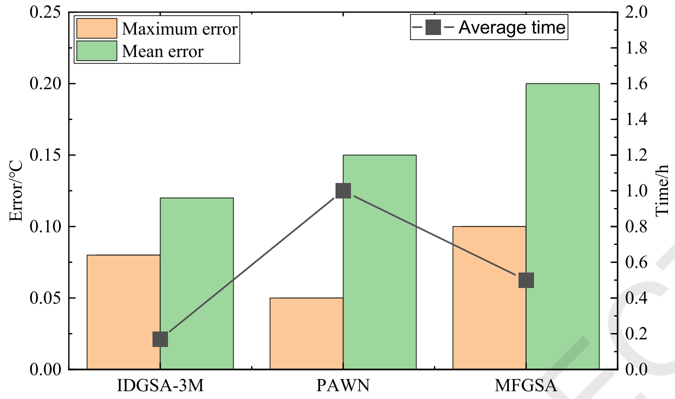

Fig. 15. Comprehensive comparison based on the three algorithms.

craft thermal analysis and design. To date, the density-based GSA of spacecraft thermal design parameters has not been studied in detail. However, it is a fundamental part of spacecraft thermal design because thermal analysis and GSA tasks are assigned in several design phases of aerospace projects.

Model reduction has a high potential to automate and reduce the cost of model evaluation, but is also a challenging topic, particularly as research on the application of thermal model reduction for spacecraft remains weak, and there is a strong demand for further extended research into engineering applications.

With model reduction, MF metamodeling can further improve the efficiency of model evaluation with high accuracy. Although there is still a lack of research on the application of MF metamodeling to spacecraft thermal analysis, there is great potential for its application and extended research on spacecraft thermal analysis.

Based on MF metamodeling, PLHS is used to sample the model parameters and terminate sampling according to demand by observing the fitting performance of modeling the RBF-IMEA surrogate to the spacecraft thermal model. This not only avoids the influence of the uncertainty of model parameters on the sampling space and GSA, but also ensures the homogeneity of the sampling space and the representativeness of the overall distribution of model parameters, which greatly improves the efficiency of sampling and model evaluation.

Density-based GSA from IDGSA-3M has a major advantage over various traditional variance-based GSA methods in terms of both the complexity and convergence of the algorithm. Moreover, the entire algorithm process is being integrated into a software platform to ease future research into its application to the optimization of spacecraft thermal design parameters. It has to be admitted that the current IDGSA-3M for engineering applications is too complex, and needs to be simplified and further improved in terms of convergence efficiency and model evaluation accuracy.

Remark. To achieve better performance, the parameters should be optimally set from four perspectives:

(i) the scaling parameters of HF and LF for MF modeling should be set to ensure accuracy and enhance the evaluation speed;
(ii) the optimization of surrogate modeling should be based on MF metamodeling and RBF-IMEA for the high-precision fitting of space thermal analysis models;
(iii) the sampling method should be selected to well avoid the influence of the uncertainty of the model parameters on the GSA and ensure the homogeneity of the sampling space of the model parameters;
(iv) the parameter settings of the density-based GSA method affect the convergence and accuracy of the final GSA index.

6. Conclusions

An intelligent density-based GSA framework based on machine learning and MF was proposed that used pared-down RTMM to reduce the cost of computing GSA but maintained accuracy through DTMM based on an intelligent batch processing system and real-time data interaction between MATLAB and NX/TMG. Then, RBF-IMEA was applied to approximate the thermophysical model of a spacecraft. Finally, the output distributions of the RBF were characterized by its CDF to obtain density-based sensitivity indices. The theoretical and experimental results proved that the evaluation effect of GSA based on IDGSA-3M was better than that of PAWN and the classical MFGSA methods based on Monte Carlo methods and manual tuning, with better model evaluation accuracy and higher computation efficiency, and better declaration of importance differences between parameters. Crucially, the entire process was automated, which helped to improve the efficiency of optimization for spacecraft thermal design.

Additionally, the convergence of IDGSA-3M was not particularly stable because the processes involved in engineering applications are complicated. However, to further improve the thermal design of the spacecraft in future research, the convergence accuracy and a simplified implementation process are indispensable for IDGSA-3M.

Declaration of competing interest

The authors declare that they have no known competing financial interests or personal relationships that could have appeared to influence the work reported in this paper.

Acknowledgements

This work was supported by the National Natural Science Foundation of China [grant number 61605203] and the Youth Innovation Promotion Association of the Chinese Academy of Sciences [grant number 2015173]. We thank Maxine Garcia, PhD, from Liwen Bianji, Edanz Group China (www.liwenbianji.cn/ac) for editing the English text of a draft of this manuscript.

References

[1] A. Saltelli, M. Ratto, T. Andres, F. Campolongo, J. Cariboni, D. Gatelli, M. Saisana, S. Tarantola, Global Sensitivity Analysis: The Primer, John Wiley & Sons, 2008.
[2] R. Loni, B. Ghobadian, A.B. Kasaeian, M.M. Akhlaghi, E. Bellos, G. Najafi, Sensitivity analysis of parabolic trough concentrator using rectangular cavity receiver, Appl. Therm. Eng. (2020) 114948, https://doi.org/10.1016/j.applthermaleng.2020.114948.
[3] W.F. Du, S. Zhuo, L. Yang, R.C. Zhao, Numerical simulation and parameter sensitivity analysis of coupled heat transfer by PCCS containment wall, Appl. Therm. Eng. 113 (2017) 867–877, https://doi.org/10.1016/j.applthermaleng.2016.11.098.
[4] R. Djeddi, K. Ekici, FDOT: a fast, memory-efficient and automated approach for discrete adjoint sensitivity analysis using the operator overloading technique, Aerosp. Sci. Technol. 91 (2019) 159–174, https://doi.org/10.1016/j.ast.2019.05.004.
[5] A. Altan, R. Hacıog, A. Altan, Model predictive control of three-axis gimbal system mounted on UAV for real-time target tracking under external disturbances, Mech. Syst. Signal Process. 138 (2020) 106548, https://doi.org/10.1016/j.ymssp.2019.106548.
[6] Modeling of three-axis gimbal system on unmanned air vehicle (UAV) under external disturbances | IEEE Conference Publication | IEEE Xplore, (n.d.), https://ieeexplore.ieee.org/document/7960196. (Accessed 6 April 2021).
[7] J. Wang, Y. Gan, J. Liang, M. Tan, Y. Li, Sensitivity analysis of factors influencing a heat pipe-based thermal management system for a battery module with cylindrical cells, Appl. Therm. Eng. 151 (2019) 475–485, https://doi.org/10.1016/j.applthermaleng.2019.02.036.
[8] W. Yun, Z. Lu, P. He, X. Jiang, Y. Dai, Parameter global reliability sensitivity analysis with meta-models: a probability estimation-driven approach, Aerosp. Sci. Technol. (2020) 106040, https://doi.org/10.1016/j.ast.2020.106040.
[9] A. Altan, Performance of metaheuristic optimization algorithms based on swarm intelligence in attitude and altitude control of unmanned aerial vehicle for path following, in: 4th Int. Symp. Multidiscip. Stud. Innov. Technol. ISMSIT 2020 - Proc., Institute of Electrical and Electronics Engineers Inc., 2020.
[10] Y. Xiong, L. Guo, Y. Huang, L. Chen, Intelligent thermal control strategy based on reinforcement learning for space telescope, J. Thermophys. Heat Transf. (2019) 1–8, https://doi.org/10.2514/1.t5774.
[11] R. Nie, B. He, S. Yan, X. Ma, Optimization design method for the cable network of mesh reflector antennas considering space thermal effects, Aerosp. Sci. Technol. 94 (2019) 105380, https://doi.org/10.1016/j.ast.2019.105380.
[12] J. Díaz, S. Hernández, Uncertainty quantification and robust design of aircraft components under thermal loads, Aerosp. Sci. Technol. 14 (2010) 527–534, https://doi.org/10.1016/j.ast.2010.04.004.
[13] T.Y. Kim, B.S. Hyun, J.J. Lee, J. Rhee, Numerical study of the spacecraft thermal control hardware combining solid-liquid phase change material and a heat pipe, Aerosp. Sci. Technol. 27 (2013) 10–16, https://doi.org/10.1016/j.ast.2012.05.007.
[14] R.G. Regis, Evolutionary programming for high-dimensional constrained expensive black-box optimization using radial basis functions, IEEE Trans. Evol. Comput. 18 (2014) 326–347, https://doi.org/10.1109/TEVC.2013.2262111.
[15] J.P.C. Kleijnen, Kriging metamodeling in simulation: a review, Eur. J. Oper. Res. 192 (2009) 707–716, https://doi.org/10.1016/j.ejor.2007.10.013.
[16] Z.H. Han, Y. Zhang, C.X. Song, K.S. Zhang, Weighted gradient-enhanced kriging for high-dimensional surrogate modeling and design optimization, AIAA J. 55 (2017) 4330–4346, https://doi.org/10.2514/1.J055842.
[17] J. Qian, J. Yi, Y. Cheng, J. Liu, Q. Zhou, A sequential constraints updating approach for Kriging surrogate model-assisted engineering optimization design problem, Eng. Comput. 36 (2020) 993–1009, https://doi.org/10.1007/s00366-019-00745-w.
[18] R. Datta, R.G. Regis, A surrogate-assisted evolution strategy for constrained multi-objective optimization, Expert Syst. Appl. 57 (2016) 270–284, https://doi.org/10.1016/j.eswa.2016.03.044.
[19] Z. Song, B.T. Murray, B. Sammakia, S. Lu, Multi-objective optimization of temperature distributions using artificial neural networks, in: Intersoc. Conf. Therm. Thermomechanical Phenom. Electron. Syst. ITHERM, 2012, pp. 1209–1218.
[20] A. Altan, O. Aslan, R. Hacioglu, Real-time control based on NARX neural network of hexarotor UAV with load transporting system for path tracking, in: 2018 6th Int. Conf. Control Eng. Inf. Technol. CEIT 2018, Institute of Electrical and Electronics Engineers Inc., 2018.
[21] R. Kromanis, P. Kripakaran, Support vector regression for anomaly detection from measurement histories, Adv. Eng. Inform. 27 (2013) 486–495, https://doi.org/10.1016/j.aei.2013.03.002.
[22] S. Rahmani, M. Ebrahimi, A. Honaramooz, A surrogate-based optimization using polynomial response surface in collaboration with population-based evolutionary algorithm, in: Adv. Struct. Multidiscip. Optim., Springer International Publishing, 2018, pp. 269–280.
[23] Q. Zhou, Y. Wang, S.K. Choi, P. Jiang, X. Shao, J. Hu, A sequential multi-fidelity metamodeling approach for data regression, Knowl.-Based Syst. 134 (2017) 199–212, https://doi.org/10.1016/j.knosys.2017.07.033.
[24] L. Le Gratiet, Recursive co-kriging model for Design of Computer experiments with multiple levels of fidelity with an application to hydrodynamic, http://arxiv.org/abs/1210.0686, 2012. (Accessed 31 March 2021).
[25] R.H. Myers, D.C. Montgomery, C.M. Anderson-Cook, Response Surface Methodology: Process and Product Optimization Using Designed Experiments, John Wiley & Sons, 2016, https://books.google.co.uk/books?id=YFSzCgAAQBAJ.
[26] Z.H. Han, S. Görtz, Hierarchical kriging model for variable-fidelity surrogate modeling, AIAA J. 50 (2012) 1885–1896, https://doi.org/10.2514/1.J051354.
[27] K.J. Chang, R.T. Haftka, G.L. Giles, P.J. Kao, Sensitivity-based scaling for approximating structural response, J. Aircr. 30 (1993) 283–288, https://doi.org/10.2514/3.48278.
[28] Y. Liu, M. Collette, Improving surrogate-assisted variable fidelity multi-objective optimization using a clustering algorithm, Appl. Soft Comput. J. 24 (2014) 482–493, https://doi.org/10.1016/j.asoc.2014.07.022.
[29] N. Van Nguyen, M. Tyan, J.W. Lee, A modified variable complexity modeling for efficient multidisciplinary aircraft conceptual design, Optim. Eng. 16 (2015) 483–505, https://doi.org/10.1007/s11081-014-9273-7.
[30] J. Zheng, X. Shao, L. Gao, P. Jiang, Z. Li, A hybrid variable-fidelity global approximation modelling method combining tuned radial basis function base and kriging correction, J. Eng. Des. 24 (2013) 604–622, https://doi.org/10.1080/09544828.2013.788135.
[31] F. Pianosi, T. Wagener, A simple and efficient method for global sensitivity analysis based on cumulative distribution functions, Environ. Model. Softw. 67 (2015) 1–11, https://doi.org/10.1016/j.envsoft.2015.01.004.
[32] Y. Zheng, C. Yan, Y. Zhao, Uncertainty and sensitivity analysis of inflow parameters for HyShot II scramjet numerical simulation, Acta Astronaut. (2019), https://doi.org/10.1016/j.actaastro.2019.12.020.
[33] F. Pianosi, K. Beven, J. Freer, J.W. Hall, J. Rougier, D.B. Stephenson, T. Wagener, Sensitivity analysis of environmental models: a systematic review with practical workflow, Environ. Model. Softw. 79 (2016) 214–232, https://doi.org/10.1016/j.envsoft.2016.02.008.
[34] S. Wang, W. Zhang, F. Cai, Q. Wang, C. Yan, Uncertainty and sensitivity study on blunt body's drag and heat reduction with combination of spike and opposing jet, Acta Astronaut. 167 (2020) 52–62, https://doi.org/10.1016/j.actaastro.2019.10.045.
[35] W. Tian, C. Jiang, B. Ni, Z. Wu, Q. Wang, L. Yang, Global sensitivity analysis and multi-objective optimization design of temperature field of sinter cooler based on energy value, Appl. Therm. Eng. 143 (2018) 759–766, https://doi.org/10.1016/j.applthermaleng.2018.08.006.
[36] G. Baroni, S. Tarantola, A general probabilistic framework for uncertainty and global sensitivity analysis of deterministic models: a hydrological case study, Environ. Model. Softw. 51 (2014) 26–34, https://doi.org/10.1016/j.envsoft.2013.09.022.
[37] I. Torralbo, I. Perez-Grande, A. Sanz-Andres, J. Piqueras, Correlation of spacecraft thermal mathematical models to reference data, Acta Astronaut. 144 (2018) 305–319, https://doi.org/10.1016/j.actaastro.2017.12.033.
[38] H. Azarkish, M. Rashki, Reliability and reliability-based sensitivity analysis of shell and tube heat exchangers using Monte Carlo simulation, Appl. Therm. Eng. 159 (2019), https://doi.org/10.1016/j.applthermaleng.2019.113842.
[39] T. Beck, B.S. Lüthi, G. Messina, D. Piazza, K. Seiferlin, N. Thomas, Thermal analysis of a reflective baffle designed for space applications, Acta Astronaut. 69 (2011) 323–334, https://doi.org/10.1016/j.actaastro.2011.03.014.

[40] H. Liu, W. Chen, A. Sudjianto, Relative entropy based method for probabilistic sensitivity analysis in engineering design, J. Mech. Des. Trans. ASME 128 (2006) 326–336, https://doi.org/10.1115/1.2159025.

[41] C.K. Park, K. Il Ahn, A new approach for measuring uncertainty importance and distributional sensitivity in probabilistic safety assessment, Reliab. Eng. Syst. Saf. 46 (1994) 253–261, https://doi.org/10.1016/0951-8320(94)90119-8.

[42] B. Krykacz-Hausmann, Epistemic sensitivity analysis based on the concept of entropy, https://www.osti.gov/etdeweb/biblio/20188282, 2001. (Accessed 31 March 2021).

[43] H. Liu, W. Chen, A. Sudjianto, Relative entropy based method for probabilistic sensitivity analysis in engineering design, J. Mech. Des. Trans. ASME 128 (2006) 326–336, https://doi.org/10.1115/1.2159025.

[44] E. Plischke, E. Borgonovo, C.L. Smith, Global sensitivity measures from given data, Eur. J. Oper. Res. 226 (2013) 536–550, https://doi.org/10.1016/j.ejor.2012.11.047.

[45] E. Borgonovo, A new uncertainty importance measure, Reliab. Eng. Syst. Saf. 92 (2007) 771–784, https://doi.org/10.1016/j.ress.2006.04.015.

[46] E. Qian, B. Peherstorfer, D. O'Malley, V.V. Vesselinov, K. Willcox, Multifidelity Monte Carlo estimation of variance and sensitivity indices, SIAM/ASA J. Uncertain. Quantificat. 6 (2018) 683–706, https://doi.org/10.1137/17M1151006.

[47] F. Pianosi, F. Sarrazin, T. Wagener, A Matlab toolbox for global sensitivity analysis, Environ. Model. Softw. 70 (2015) 80–85, https://doi.org/10.1016/j.envsoft.2015.04.009.

[48] K. Stout, Bayesian-based simulation model validation for spacecraft thermal systems, https://dspace.mit.edu/handle/1721.1/97358, 2015. (Accessed 25 November 2019).

[49] D.P. Thunnissen, G.T. Tsuyuki, Margin determination in the design and development of a thermal control system, SAE Transact. 113 (2004) 899–916, https://doi.org/10.2307/44737952.

[50] X. He, J. Zeng, X. Y, RBF neural network structure optimization based on MEC algorithm, Comput. Eng. 30 (2004) 72–78, http://en.cnki.com.cn/Article_en/CJFDTotal-JSJC200409028.htm. (Accessed 28 November 2019).

[51] L. Yanqing, D. Yingying, Short-term photovoltaic power forecasting based on optimal similarity and radial basis function neural networks optimized by improved mind evolutionary algorithm, J. North China Electr. Power Univ. 45 (2018) 29–36, https://doi.org/10.3969/j.ISSN.1007-2691.2018.05.04.

[52] L. Shu, P. Jiang, X. Song, Q. Zhou, Novel approach for selecting low-fidelity scale factor in multifidelity metamodeling, AIAA J. (2019) 1–11, https://doi.org/10.2514/1.j057989.

[53] Q. Zhou, Y. Yang, P. Jiang, X. Shao, L. Cao, J. Hu, Z. Gao, C. Wang, A multi-fidelity information fusion metamodeling assisted laser beam welding process parameter optimization approach, Adv. Eng. Softw. 110 (2017) 85–97, https://doi.org/10.1016/j.advengsoft.2017.04.001.

[54] L. Shu, P. Jiang, Q. Zhou, X. Shao, J. Hu, X. Meng, An on-line variable fidelity metamodel assisted multi-objective genetic algorithm for engineering design optimization, Appl. Soft Comput. J. 66 (2018) 438–448, https://doi.org/10.1016/j.asoc.2018.02.033.

[55] J. Ollar, C. Mortished, R. Jones, J. Sienz, V. Toropov, Gradient based hyper-parameter optimisation for well conditioned kriging metamodels, Struct. Multidiscip. Optim. 55 (2017) 2029–2044, https://doi.org/10.1007/s00158-016-1626-8.

[56] Z. Yechi, Z. Long, L. Wenbo, P. Teng, Rapid thermal information analysis of on-orbit satellites on the basis of statistic method, Chin. Sp. Sci. Technol. 36 (2016) 55–61, https://doi.org/10.16708/j.cnki.1000-758X.2016.0062.

[57] G.L. Somma, H.G. Lewis, C. Colombo, Sensitivity analysis of launch activities in low Earth orbit, Acta Astronaut. 158 (2019) 129–139, https://doi.org/10.1016/j.actaastro.2018.05.043.

[58] D. Cui, J. Zhao, S. Yan, X. Guo, J. Li, Analysis of parameter sensitivity on dynamics of satellite separation, Acta Astronaut. 114 (2015) 22–33, https://doi.org/10.1016/j.actaastro.2015.04.007.

[59] E. Borgonovo, Measuring uncertainty importance: investigation and comparison of alternative approaches, Risk Anal. 26 (2006) 1349–1361, https://doi.org/10.1111/j.1539-6924.2006.00806.x.

[60] Q. Liu, T. Homma, A new computational method of a moment-independent uncertainty importance measure, Reliab. Eng. Syst. Saf. 94 (2009) 1205–1211, https://doi.org/10.1016/j.ress.2008.10.005.

[61] W. Castaings, E. Borgonovo, M.D. Morris, S. Tarantola, Sampling strategies in density-based sensitivity analysis, Environ. Model. Softw. 38 (2012) 13–26, https://doi.org/10.1016/j.envsoft.2012.04.017.

[62] E. Borgonovo, A new uncertainty importance measure, Reliab. Eng. Syst. Saf. 92 (2007) 771–784, https://doi.org/10.1016/j.ress.2006.04.015.

[63] W. Xiang, S. Yan, Dynamic analysis of space robot manipulator considering clearance joint and parameter uncertainty: modeling, analysis and quantification, Acta Astronaut. 169 (2020) 158–169, https://doi.org/10.1016/j.actaastro.2020.01.011.

[64] A. Gómez-San-Juan, I. Pérez-Grande, A. Sanz-Andrés, Uncertainty calculation for spacecraft thermal models using a generalized SEA method, Acta Astronaut. 151 (2018) 691–702, https://doi.org/10.1016/j.actaastro.2018.05.045.

[65] J. Roshanian, M. Ebrahimi, Latin hypercube sampling applied to reliability-based multidisciplinary design optimization of a launch vehicle, Aerosp. Sci. Technol. 28 (2013) 297–304, https://doi.org/10.1016/j.ast.2012.11.010.

[66] R. Sheikholeslami, S. Razavi, Progressive Latin hypercube sampling: an efficient approach for robust sampling-based analysis of environmental models, Environ. Model. Softw. 93 (2017) 109–126, https://doi.org/10.1016/j.envsoft.2017.03.010.

[67] S.M. Attaran, R. Yusof, H. Selamat, A novel optimization algorithm based on epsilon constraint-RBF neural network for tuning PID controller in decoupled HVAC system, Appl. Therm. Eng. 99 (2016) 613–624, https://doi.org/10.1016/j.applthermaleng.2016.01.025.

[68] S. Chengyi, X. Keming, C. Mingqi, Mind evolution based machine learning framework and new development, J. Taiyuan Univ. Technol. 30 (1999) 453–457, http://www.cqvip.com/qk/90007a/199905/3768392.html. (Accessed 20 December 2019).

[69] J.A. Richmond, Adaptive Thermal Modeling Architecture for Small Satellite Applications, Massachusetts Institute of Technology, 2010.

[70] R. Kovàcs, V. Józsa, Thermal analysis of the SMOG-1 PocketQube satellite, Appl. Therm. Eng. 139 (2018) 506–513, https://doi.org/10.1016/j.applthermaleng.2018.05.020.

[71] The Monte Carlo Ray-Trace Method in Radiation Heat Transfer and Applied Optics | Wiley, (n.d.), https://www.wiley.com/en-us/The+Monte+Carlo+Ray+Trace+Method+in+Radiation+Heat+Transfer+and+Applied+Optics-p-9781119518501. (Accessed 4 April 2021).

[72] M. Deiml, M. Suderland, P. Reiss, M. Czupalla, Development and evaluation of thermal model reduction algorithms for spacecraft, Acta Astronaut. 110 (2015) 168–179, https://doi.org/10.1016/j.actaastro.2015.01.018.